Article

Kirigami-inspired parachutes with programmable reconfiguration

https://doi.org/10.1038/s41586-025-09515-9

Received: 10 July 2024

Accepted: 11 August 2025

Published online: 1 October 2025

Check for updates

Danick Lamoureux[1], Jérémi Fillion[1], Sophie Ramananarivo[2], Frédérick P. Gosselin[1]✉ & David Melancon[1]✉

The art of kirigami allows programming a sheet to deform into a particular manner with a pattern of cuts, endowing it with exotic mechanical properties and behaviours[1–17]. Here we program discs to deform into stably falling parachutes as they deploy under fluid–structure interaction. Parachutes are expensive and delicate to manufacture, which limits their use for humanitarian airdrops or drone delivery. Laser cutting a closed-loop kirigami pattern[18] in a disc induces porosity and flexibility into an easily fabricated parachute. By performing wind tunnel testing and numerical simulations using a custom flow-induced reconfiguration model[19], we develop a design tool to realize kirigami-inspired parachutes. Guided by these results, we fabricate parachutes from the centimetre to the metre scale and test them in realistic conditions. We show that at low load-to-area ratios, kirigami-inspired parachutes exhibit a comparable terminal velocity to conventional ones. However, unlike conventional parachutes that require a gliding angle for vertical stability[20] and fall at random far from a target, our kirigami-inspired parachutes always fall near the target, regardless of their initial release angle. These kinds of parachutes could limit material losses during airdropping as well as decrease manufacturing costs and complexity.

The art of kirigami, in which cutting paper leads to complex shape morphing, has recently been exploited by researchers[1–3] to design deployable structures with programmable deformation[4–6], coupling stretching, twisting and bending[7–10], auxeticity[11–13] and nonlinear behaviour[14–17]. Although kirigami structures are typically deployed manually, recent studies have shed light on their complex fluid–structure interactions (FSI)[21,22], which can be harnessed for aerodynamic control[23–25].

When subjected to incoming flow, a slender elastic structure such as a tree leaf[26], a sheet of polymer[27–29] or a kirigami motif[21] can deform with large amplitude and affect the scaling of the drag with the flow velocity. This flow-induced reconfiguration[30,31] is commonly found in nature, for example, trees[32], leaves[26,28,31] and aquatic plants[33,34], as well as in engineering applications, including draping discs that exhibit multiple stable states[35], kirigami sheets that can tune porosity and permeability[21,22], passive actuation[36] and energy harvesting[37]. Here we focus on the closed-loop kirigami pattern[18] (Fig. 1a) and, taking inspiration from wind-dispersal seeds[38] and deciduous tree leaves[39], we build kirigami-inspired parachutes that exploit their quasi-axisymmetric deformation under flow to program the aerodynamic stability of thin circular sheets in free fall. Although leveraging kirigami principles to deploy shapes and objects under mechanical[7,40] and fluid[21,22] actuation has been studied, we apply these concepts to the design and deployment of kirigami-inspired parachutes, a direction that, to our knowledge, has not been previously explored.

First, we study the free-falling motion of kirigami discs and highlight the impact of the cut pattern on the deployed shape and lateral drift. We then quantify experimentally the deployment and drag of our structures using a wind tunnel to apply a uniform flow. By combining analytical models based on beam formulations and finite element simulations using a custom flow-induced reconfiguration model (FIRM)[19], we present a methodology to program the reconfiguration of closed-loop kirigami discs under flow. Finally, we build kirigami-inspired parachutes and characterize their flight performance by dropping them indoors above a target and outdoors from a drone to deliver a bottle of water.

Free fall of flexible kirigami discs

To study the influence of the kirigami pattern on the kinematics of the disc during free fall, we performed laser cutting of three different geometries. As a baseline, the first disc has no cuts. We then fabricate two discs with distinct kirigami patterns, which we call design A and design B (see Methods and Extended Data Fig. 1 for more details on the kirigami pattern geometries). To guide the fall of each disc, we fix a payload consisting of a screw and a bolt with a mass of 4.5 g. When dropped from an initial height of 1.8 m, both the disc with no cuts and design A deform into a cylindrical mode as previously described[35] (referred to as mode $\mathcal{C}$), which is reminiscent of a draping disc under flow[35,41]. As highlighted from the snapshots in Fig. 1b,c, this mode of deformation does not provide stability during the fall and the discs tumble, a behaviour that has been observed in previous works[42,43]. When launched from the same initial height, design B undergoes an elongation that remains aligned with the vertical axis during the entire fall (see snapshots in Fig. 1d and Supplementary Video 1). This quasi-axisymmetric mode of deformation of the closed-loop pattern (referred to as mode $\mathcal{K}$) has

[1]Laboratory for Multiscale Mechanics (LM2), Department of Mechanical Engineering, Research Center for High Performance Polymer and Composite Systems (CREPEC), Polytechnique Montreal, Montreal, Quebec, Canada. [2]LadHyX, CNRS, École Polytechnique, Institut Polytechnique de Paris, Palaiseau, France. ✉e-mail: frederick.gosselin@polymtl.ca; david.melancon@polymtl.ca

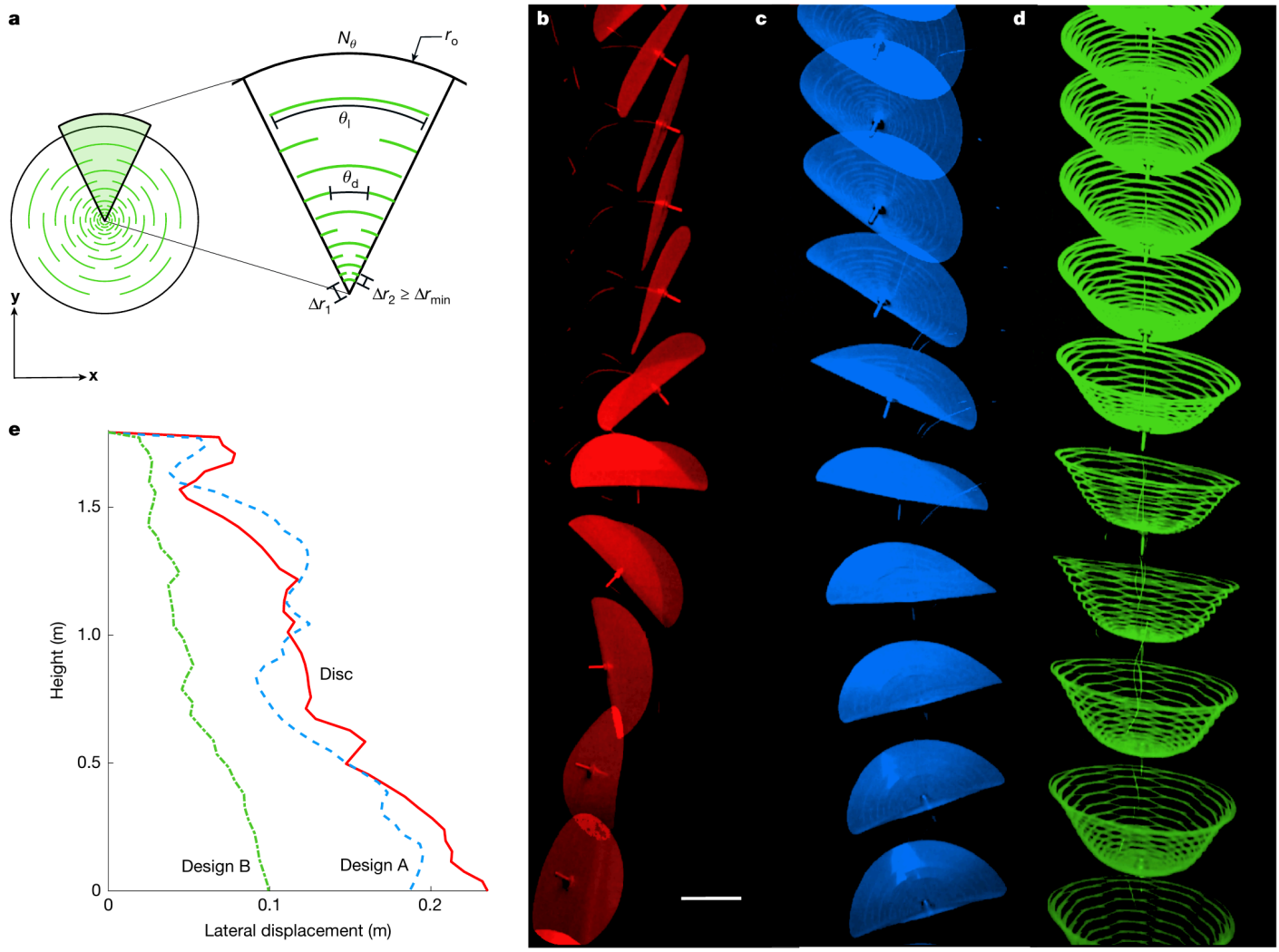

Fig. 1 | Kinematics of free-falling kirigami discs. a, Schematic of the closed-loop kirigami pattern made of N_θ identical sectors of a disc of external radius r_o and thickness t with cuts spanning an angle θ_l spaced from each other by θ_d along the circumference, with $\Theta = \theta_d/\theta_l$, and Δr_j along the radius. The radial spacing Δr_j is defined using the initial spacing Δr_2 and the distribution exponent n, such that $\Delta x_{j+1} = \Delta r_{j+1}/r_0 = (1 + \Delta x_j)^n - 1 \; \forall j \geq 2$, with the first cut at Δr_1 from the inner radius r_i. **b**–**d**, Snapshots of three discs with thickness $t = 69$ µm, $r_o = 70$ mm and $r_i = 3$ mm during free fall. A disc with no cuts and discs with a kirigami pattern defined with $\Delta r_1 = 3$ mm, $\Delta r_2 = 2$ mm, $n = 1$, $\Theta = 0.3$ (**b**); $N_\theta = 8$ (design A) (**c**); and $N_\theta = 5$ (design B) (**d**). **e**, Three standard deviations of the lateral displacement as a function of vertical height during free fall for the disc with no cuts, design A and design B. The lines represent three times the absolute standard deviation of 10 drop tests for each disc. Scale bar, 50 mm (**b**–**d**).

been reported previously for discs under displacement or force loading[8,18,22,44,45]. To quantify the repeatability of the free-falling motion of the kirigami discs, we repeat the drop test on each geometry 10 times while tracking the lateral displacement as a function of the height. The curves in Fig. 1e represent three times the envelope of the standard deviation for the disk with no cuts, design A and design B. The results confirm that design B has the lowest lateral drift after the fall.

Kirigami reconfiguration under flow

Inspired by the impact of the kirigami pattern on the vertical stability of discs during free fall, we subject the previously manufactured discs to a uniform air flow of speed U_∞ in a wind tunnel (Methods and Supplementary Video 2). Figure 2a,b shows the snapshots of designs A and B at increasing flow velocities. We note the same reconfiguration in the wind tunnel and the free fall, that is, designs A and B deform into modes $\mathcal{C}$ and $\mathcal{K}$, respectively. Figure 2c,d shows the elongation w (defined as the distance along the z-axis between the inner and outer radii of the disc) and the drag D (defined as the measured force along the z-axis) as a function of U_∞ for design A (blue continuous line) and design B (green continuous line). The circular and diamond markers correspond to the snapshots in Fig. 2a,b, respectively. For the same flow velocity U_∞, design B elongates more than design A (see w–U_∞ curves in Fig. 2c). This is due to two contributions. First, design B shows a softer response under uniaxial extension compared with design A (Methods and Extended Data Fig. 5), thus allowing a higher elongation. Second, the maximum extension of mode $\mathcal{K}$ of design B is dictated by the added length of each beam (see Supplementary Methods, section S2C, for more details), whereas, for mode $\mathcal{C}$ of design A, this limit is given by $r_o - r_i$. Although their deformation under flow differs, the drag generated by designs A and B is similar and smaller than that of a rigid disc because of reconfiguration (Fig. 2d, continuous black line). Similar to a leaf bending and twisting under the wind[26], the kirigami discs reduce their cross-sectional area perpendicular to the flow and become more streamlined as their components become aligned with the flow[31]. Apart from these two mechanisms of drag reduction, there is also an opening of the pores of the kirigami discs, which occurs as they deform, which modifies the effective flow speed.

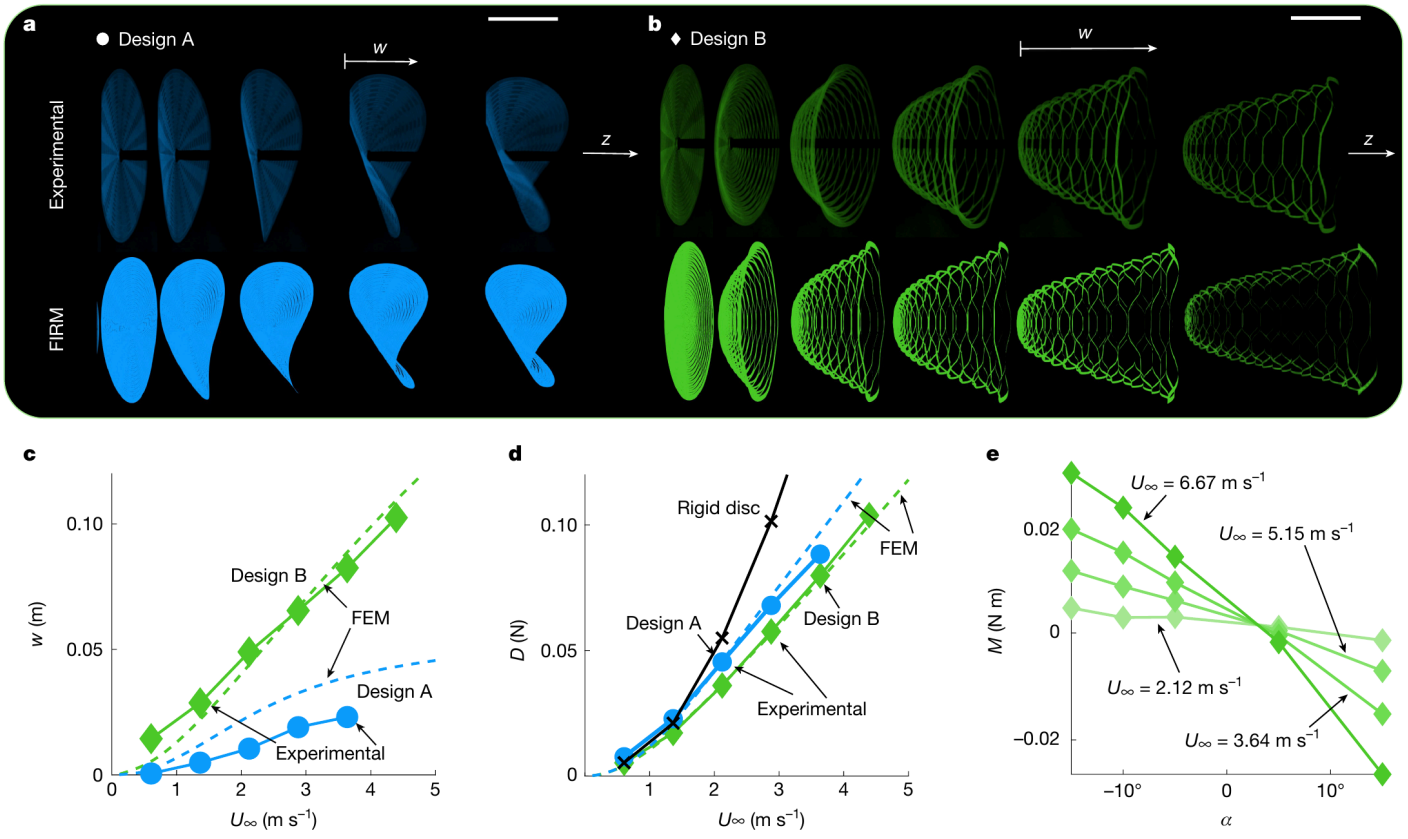

Fig. 2 | Reconfiguration of kirigami discs under flow. a,**b**, Snapshots of kirigami discs design A and design B reconfiguring under flow during a wind tunnel experiment (top) and as predicted numerically by our custom FIRM (bottom). **c**,**d**, Evolution of axial elongation w (**c**) and drag D (**d**) as a function of flow velocity U_∞. Both experimental (continuous lines) and numerical (dashed lines) are reported in **c** and **d**. Displacements are measured from pictures, and drag is averaged over a 30-s period in the wind tunnel. The markers identify the velocities of the snapshots highlighted in **a** and **b**. **e**, Measured aerodynamic moment M generated by the kirigami disc design B as a function of the angle of attack with the flow α. The different continuous lines correspond to experimental measurements at different velocities, and the markers are averages over a 30-s period in the wind tunnel. Scale bars, 50 mm (**a**,**b**).

When we compare these experimental results with our numerical simulations performed using the FIRM framework[19], we find an excellent agreement, both qualitatively (see numerical snapshots in Fig. 2a,b at the same fluid velocity) and quantitatively (dashed lines in Fig. 2c,d and Methods). It is important to note that the simulations did not take the deformation mode as an input, yet they accurately predicted the deformation mode in all cases we tested.

From the free-falling and wind tunnel tests, we note that, when deforming in mode $\mathcal{K}$, the large extension has an important contribution to the stability of the disc. We believe that this is due to a lever effect that helps in generating a stabilizing moment for the disc. To verify this hypothesis, we measure, in the wind tunnel, the moment M generated by design B for different angles of attack, α and velocities (Fig. 2e (green continuous lines), in which the shading corresponds to different values of U_∞). We note that all the M–α curves are decreasing such that $\mathrm{d}M/\mathrm{d}\alpha < 0$, which leads to statically stable falling dynamics. Moreover, we see that at higher velocities, the slope of the moment becomes larger, thus increasing the stability of the discs.

To better understand how to obtain kirigami discs that deform in mode $\mathcal{K}$, we manufacture 24 specimens in a parametric sweep, varying one parameter from design B at a time (see the Methods for a complete list of kirigami discs manufactured). We then perform a tensile test on all these kirigami discs (see Extended Data Fig. 4 for the full traction curves) and measure their stiffness K. To gain more insight into the impact of geometrical parameters on the stiffness of the kirigami discs, we develop an analytical model based on an assembly of Euler–Bernoulli beams and compute their theoretical stiffness $\overline{K}$ (see Supplementary Methods, section S2B, for more details regarding the analytical model). Through this modelling procedure, we find that the total stiffness of the structure comes from three contributions: (1) the material bending stiffness B; (2) the external radius r_o of the disc; and (3) the added stiffness $\overline{K}$ of the cut pattern (see Supplementary Methods, section S2B, for the expression of $\overline{K}$). Figure 3a shows the experimentally measured stiffness according to the theoretically predicted stiffness, in which we find that $K \sim \overline{K} = B\overline{K}/r_o^2$ because the slope of the fit is close to unity. Therefore, our theoretical model can be used to predict the kirigami disc stiffness under extension.

This added stiffness of the modelled pattern can be used to define a linear transition criterion: when mode $\mathcal{K}$ is softer than mode $\mathcal{C}$, then mode $\mathcal{K}$ prevails. We find that this stiffness criterion scales as $\overline{K} \leq 28$, which is identified empirically (see Supplementary Methods, section S2D, for more details regarding the transition criterion). To validate this transition criterion, we plot in Fig. 3b the pattern added stiffness $\overline{K}$ of 24 different kirigami discs and highlight in blue and green if their observed deformation is mode $\mathcal{C}$ or $\mathcal{K}$, respectively.

Using our transition criterion, we characterize the extension and drag of each of the discs in our parametric study that deform initially in mode $\mathcal{K}$ (see Extended Data Figs. 6 and 7 for the complete drag and extension curves of the different specimens). The dimensionless numbers that describe the behaviour of the closed-loop kirigami specimens under flow are (1) the aspect ratio $l = L_e/r_o$, which defines a normalized maximum elongation measure with L_e the theoretical maximum extension length; (2) the Cauchy number $C_\gamma = \rho U_\infty^2 r_o^2 C_D/KL_e$, which compares aerodynamic loading to typical elastic restoring forces; (3) the normalized extension $\delta = w/L_e$; and (4) the reconfiguration number $\mathcal{R} = D/D_{rigid}$, where D_{rigid} is the drag of a rigid disc in the

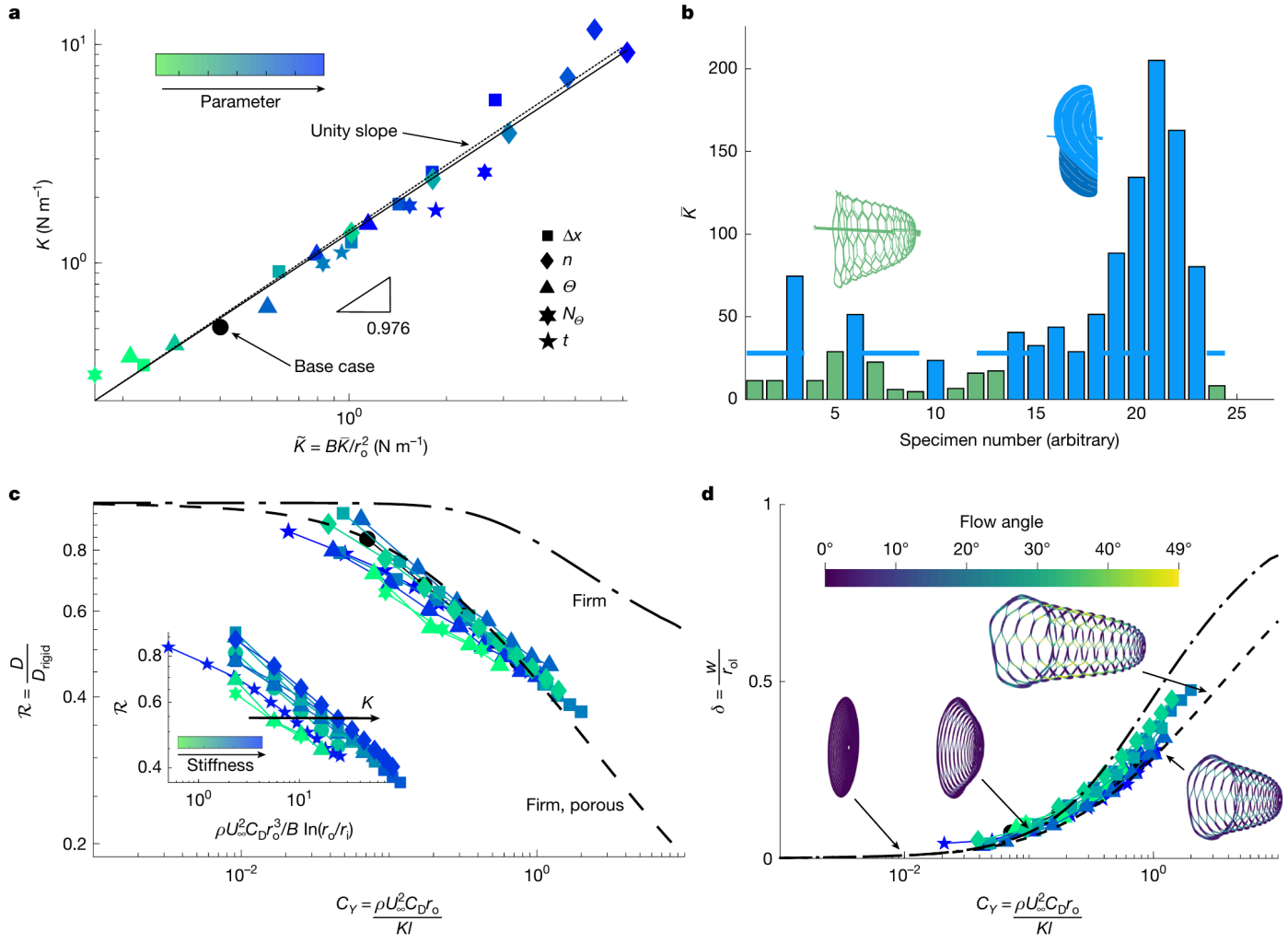

Fig. 3 | Design space of the kirigami discs. a, Theoretical stiffness modelling of the kirigami specimens, where K is the experimental stiffness in a tensile test, $\bar{K}$ is the theoretical stiffness, B is the bending stiffness, r_o is the external radius and $\bar{K}$ is the added stiffness of the kirigami pattern. **b**, Transition criterion applied to the different specimens. Tested specimens are arbitrarily ordered, and the added stiffness $\bar{K}$ of their pattern is measured and compared with the transition criterion (dashed horizontal line). **c**, Reconfiguration number, $\mathcal{R}$, of the kirigami specimens deforming in mode $\mathcal{K}$ according to the Cauchy number, C_Y, studied experimentally, over a wide range of specimens, and numerically, with and without the porosity model based on ref. 46 when simulating design B. The inset shows the reconfiguration number of the experimentally tested disc according to the Cauchy number of a draping disc[35], showing a scatter according to the experimental stiffness of the specimen. **d**, Dimensionless displacement, δ, of the kirigami specimens deforming in mode $\mathcal{K}$ as a function of the Cauchy number for experimental and numerical results with and without porosity. The accompanying snapshots show the deformed disc at different extension lengths, and their colour map shows the angle the normal of the structure makes with the flow, with the colour scale at the top of the plot in degrees.

same conditions, which allows us to compare actual drag with the rigid case. Figure 3c shows the $\mathcal{R} - C_Y$ curve of our specimens on a logarithmic scale. Experimentally, we see that the reconfiguration number of each specimen decreases as the Cauchy number increases. Moreover, we see that at low Cauchy numbers, that is, $C_Y \in [0, 2 \times 10^{-2}]$, their reconfiguration tends towards unity, which indicates a behaviour similar to a rigid body, which is expected[29]. However, at higher Cauchy numbers, that is, $C_Y \in [1 \times 10^{-1}, 100]$, $\mathcal{R}$ tends towards a constant slope in logarithmic scale, such that the drag follows a constant power law according to the velocity. This is well known in reconfiguration problems, such that $D \sim U_\infty^{2+\mathcal{V}}$, where $\mathcal{V}$ is the Vogel's exponent[26]. In our case, we find $\mathcal{V} \cong -0.279$, which means that the drag of our structure grows more slowly than a rigid structure. We note that the different kirigami specimens tested fall onto a master curve with little scatter using the reported dimensionless numbers. To showcase the impact of the cut pattern, we also plot in Fig. 3c (inset) the experimental reconfiguration number of our kirigami discs using the Cauchy number of a flexible disc without any cuts[35]. The results indicate that the data are scattered according to the stiffness of the different specimens.

Therefore, the aerodynamic behaviour of our specimens is dictated by the stiffness added by the kirigami pattern. We also plot the reconfiguration number according to the Cauchy number obtained from simulating design B using the FIRM framework. We first plot the results without considering porosity in a dash-dot line and see that the predicted reconfiguration number is higher than the experimentally measured one, that is, we predict a higher drag than the one measured. However, when the discs deform in mode $\mathcal{K}$, they elongate, which will force the slits to open, creating pores in the structure. By considering a porosity model based on ref. 46 (Methods), we plot a second curve in the dashed line that is in excellent agreement with our experimental results. This porosity could also explain the small experimental scatter that persists after normalization, as it can induce complex flow phenomena that are not considered. The reconfiguration curve shown here can be used as a tool to design the best free-falling parachute for a given disc. To maximize drag and ensure free-fall stability in a deployed state, the Cauchy number should be minimized while respecting the constraint that $\bar{K} \leq 28$ using an appropriate kirigami pattern.

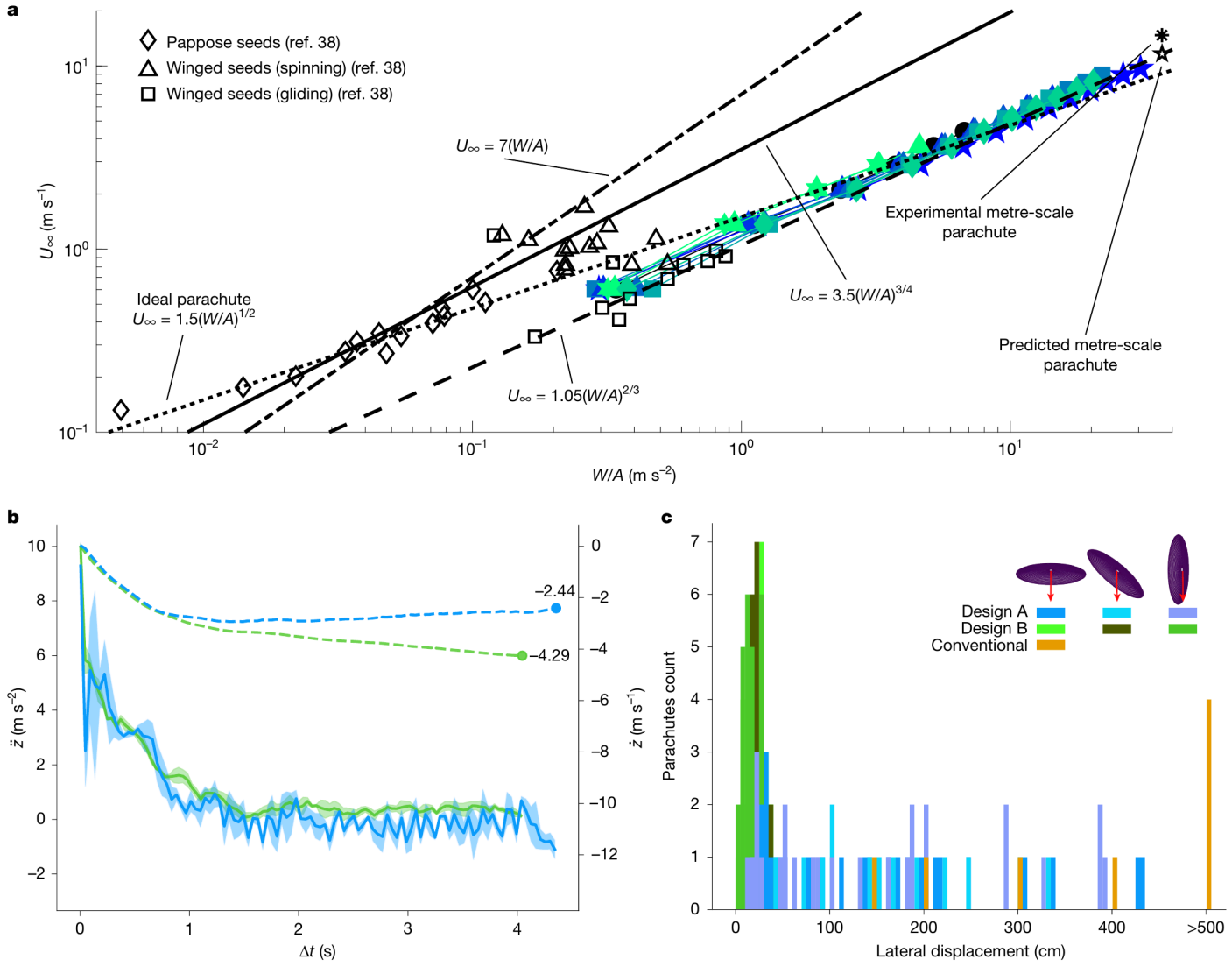

Fig. 4 | Performance of kirigami-inspired parachutes. a, Terminal velocity U_∞ as a function of load per unit of area W/A for different species of wind-dispersal seeds[38] and our kigirami-inspired parachutes (coloured markers, with the same colours that were used in Fig. 3a). The lines are trends and fits identified in ref. 38, with the black dotted line indicating the relationship of an ideal parachute. The black asterisk and star are the experimental and predicted terminal velocities of the metre-scale parachute discussed in this work. **b**, Vertical acceleration, $\ddot{z}$, and velocity, $\dot{z}$, of kirigami-inspired parachute designs A and B (blue and green, respectively). The solid lines and shaded areas are the average and standard deviation of the vertical acceleration of three fall experiments measured with an accelerometer. The dashed lines are the vertical velocity obtained by integrating numerically the mean vertical acceleration of three fall experiments. **c**, Lateral displacement across multiple drop tests of kirigami-inspired parachute designs A and B as well as a small-scale elliptical parachute (orange bars) manufactured by Fruity Chutes with $r_o = 195$ mm, $r_i = 24$ mm and a drag coefficient of $C_D = 1.5$ (Methods). The coloured bars represent parachutes launched at 0°, 45° and 90°.

We plot the normalized extension of our specimens δ according to the Cauchy number C_Y in Fig. 3d, using our experiments and different numerical results when simulating design B. Experimentally, we see that δ increases with C_Y and once again collapses on a master curve. When we overlay the simulation curves, we find that the experimental data fall between the predictions of FIRM with and without the porosity model (dash-dot and dash lines, respectively in Fig. 3d). Along the dash curve representing the FIRM simulation, we show different snapshots of the kirigami disc at different elongations along with a colour map of the angle the normal to the discs make with the flow. We see that most of the disc remains perpendicular to the flow (their normal is parallel to the flow, causing a flow angle of 0°), and only the blades generate a flow angle as the disc elongates. This deformation mode, therefore, limits the drag reduction through both profiling and area reduction[31], which explains why, at similar stiffness, a disc deforming in mode $\mathcal{K}$ would generate more drag than a disc deforming in mode $\mathcal{C}$.

We note that the elongation law can also be used to ensure parachute stability. If the parachute does not extend enough during falling, then the aerodynamic moment generated might not be sufficient to ensure vertical falling and could behave as a rigid falling disc, which is known to tumble[43].

Kirigami-inspired parachutes

The terminal velocity, U_∞, of our kirigami discs is characterized by their weight to area ratio, W/A, and can be compared with wind-dispersal seeds as well as conventional parachutes (Fig. 4a). From static equilibrium at a constant flow velocity U_∞ during the wind tunnel test, we set the measured drag, D, equal to a payload of weight, W, and plot in Fig. 4a the U_∞–W/A relation of each kirigami specimen with coloured markers. We also plot, in comparison, the behaviour of flying seeds such as the Pappose seeds, and spinning and gliding winged seeds[38]. In ref. 38, the

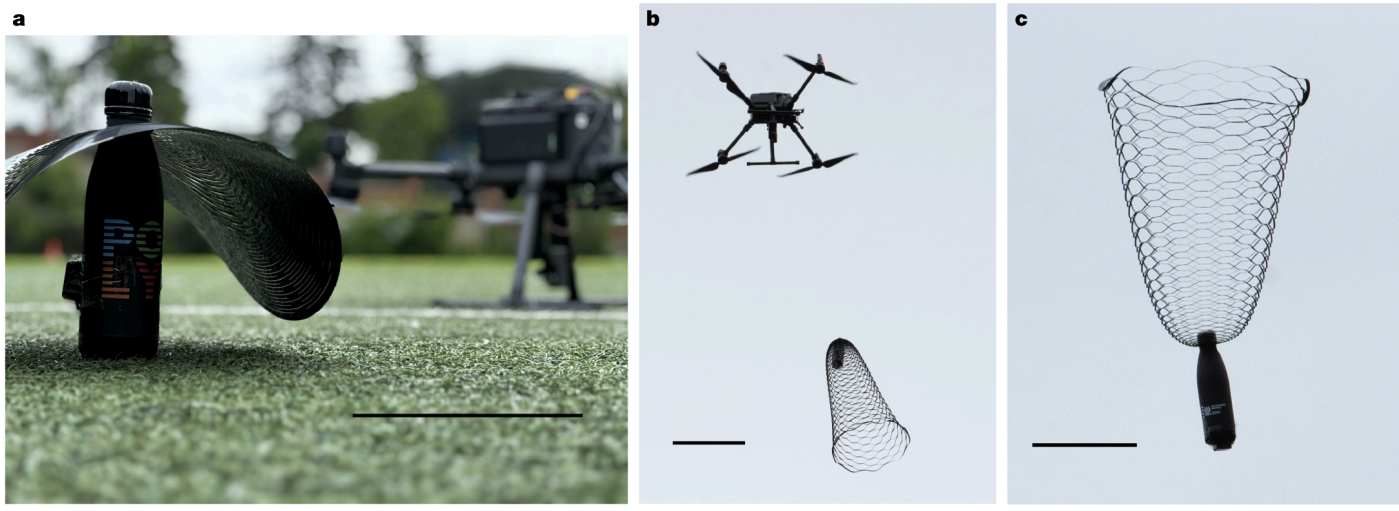

Fig. 5 | Kirigami-inspired parachutes in realistic conditions. a, Water bottle mounted on a kirigami-inspired parachute attached to a drone. **b**, Parachute elongating as the drone pulls it up to its dropping altitude of 60 m. **c**, Snapshot of a kirigami-inspired parachute during free fall in realistic conditions. Scale bars, 250 mm (**a**,**c**); 500 mm (**b**).

authors found different scaling laws, as identified in Fig. 4a, for the flying seeds, in which we happen to fit the most efficient trend as $U_\infty = 1.05(W/A)^{2/3}$. These natural flyers and our kirigami discs match conventional parachutes at low W/A, because the latter are typically modelled using $W = 1/2\rho U_\infty^2 A C_D$. This typical drag law leads to $U_\infty = (2W/\rho A C_D)^{1/2}$, which, when using the rigid disc from our experiment, the terminal velocity is described as $U_\infty = 1.5(W/A)^{1/2}$, because $C_D = 1.26$, the drag coefficient obtained experimentally, and $\rho = 1.225\ \mathrm{kg\ m^{-3}}$, the density of air. Although for high W/A, conventional parachutes achieve a lower terminal velocity compared with our kirigami discs, they require a gliding angle for vertical stability[20]. This leads to an important lateral drift when launched above a target (Fig. 4c). Moreover, their manufacturing involves complex assembly and folding. In comparison, kirigami parachutes could be easily mass-produced by simple die cutting. This could be especially relevant in the context of humanitarian airdropping, in which current parachute design and fabrication still require skilled manufacturers[47].

We then characterize the free-flight ability of kirigami-inspired parachutes based on designs A and B (Methods). We launch each parachute three times indoors from a height of 14.9 m and record their lateral, $\ddot{x}$ and $\ddot{y}$, and vertical, $\ddot{z}$, accelerations. Figure 4b shows the vertical acceleration, $\ddot{z}$, as a function of time (lateral accelerations and tumbling frequencies are reported in Extended Data Fig. 8). We find that design A (solid blue curve), deforming in mode $\mathcal{C}$, descends with an unsteady vertical acceleration. In comparison, the acceleration of design B (solid green curve), deforming in mode $\mathcal{K}$, plateaus after 2 s of flight. By integrating the average of the vertical acceleration $\ddot{z}$, we can obtain the vertical velocity $\dot{z}$ over time (Fig. 4b, dashed lines). The results indicate that the terminal velocity is $U_\infty = 2.44\ \mathrm{m\ s^{-1}}$ for design A and $U_\infty = 4.29\ \mathrm{m\ s^{-1}}$ for design B. In comparison, the terminal velocity of free fall from a height of 14.9 m is $U_\infty = 17.1\ \mathrm{m\ s^{-1}}$.

Apart from their deceleration during free fall, we characterize the lateral drift of designs A and B in a flight situation. For this purpose, we drop multiple parachutes from a height of 16.6 m with three initial release angles: 0°, 45° and 90°. We then measure the distance between the landing spot of each parachute and a ground target representing the initial release position. Figure 4c shows the distribution of the lateral displacement during the drop tests for parachute design A and design B launched at 0°, 45° and 90°. Coherent with the acceleration results, we observe that design A, while reaching a lower terminal velocity, shows a random distribution of lateral drift. This situation is similar to that of a conventional parachute, which also exhibits substantial lateral drift during free fall (see orange curves and bars in Fig. 4c and Extended Data Fig. 9). By contrast, we observe that design B consistently falls close to the target, regardless of the initial release angle (Fig. 4c). This highlights that kirigami-inspired parachutes deforming in mode $\mathcal{K}$ can quickly reach terminal velocity, provide increased stability and drop near intended targets if used to deliver humanitarian aid.

Finally, to demonstrate the concept of a kirigami-inspired parachute that can deliver humanitarian aid, we manufacture a 0.5 m diameter kirigami disc that deforms in mode $\mathcal{K}$ (Methods). We attach a water bottle to the parachute (Fig. 5a) and drop it from a drone from a height of 60 m multiple times, as shown in Fig. 5b,c and Supplementary Video 4. Based on the elongation of the parachute in Fig. 5c, we calculate a terminal velocity equal to $U_\infty = 14.1\ \mathrm{m\ s^{-1}}$ (FIRM predicted $U_\infty = 11.7\ \mathrm{m\ s^{-1}}$; Methods). In comparison, the terminal velocity reached during free fall from a height of 60 m is $34.3\ \mathrm{m\ s^{-1}}$. The predicted and experimental terminal velocity of the metre-scale parachutes are added as a comparison in Fig. 4a to show that the parachute remains on the same line as the tested kirigami discs.

Conclusions and outlook

With inspiration from kirigami, we showed that introducing cuts into thin circular sheets can lead to the design of stable parachutes to deliver humanitarian aid. Through experiments and simulations, we provided a rational strategy to trigger flow-induced reconfiguration leading to an unstable cylindrical mode of deformation (mode $\mathcal{C}$) and a stable mode of deformation (mode $\mathcal{K}$) under flow. Inspired by our simple manufacturing technique, we fabricated a large-scale kirigami parachute that successfully delivered a water bottle from a drone flying at an altitude of 60 m. We found the same reconfiguration behaviour in our kirigami discs across scales (from the centimetre scale to the metre scale) and environmental conditions (from a free fall test in the laboratory to a closed wind tunnel experiment and an outdoor test with realistic conditions). Through dimensional analysis, we showed that this behaviour depends on the added stiffness $\bar{K}$ of the kirigami pattern. Moreover, the reconfiguration of our structures can be adequately predicted by our FIRM framework, a custom corotational finite element solver. Apart from being easy to fabricate, our parachute reduces lateral displacement during descent, unlike conventional designs that often drift randomly and far from an intended target. This could be especially useful for humanitarian aid delivery. Scaling up our manufacturing

process without requiring manual assembly (Extended Data Fig. 2 and Supplementary Video 3) would be possible with industrial-size laser cutters and cutting dies. Although our software cannot evaluate the stabilizing moment numerically, it could be adapted to take circulation into account. Moreover, the terminal velocity of our kirigami-inspired parachute could be reduced by covering the cuts with a soft and highly stretchable membrane to limit the impact of porosity. Although this study focuses on the closed-loop kirigami pattern, expanding the geometrical parameter space to other designs, such as asymmetric, chiral or hierarchical patterns, could enable programming the entire fall trajectory of parachutes. Moreover, using multiple patterns of our kirigami-inspired parachute in a single launch could be used to sort out different populations during flight (Supplementary Video 5). Finally, origami could be exploited to fold the kirigami parachute for compactness.

Online content

Any methods, additional references, Nature Portfolio reporting summaries, source data, extended data, supplementary information, acknowledgements, peer review information; details of author contributions and competing interests; and statements of data and code availability are available at https://doi.org/10.1038/s41586-025-09515-9.

1. Zhai, Z., Wu, L. & Jiang, H. Mechanical metamaterials based on origami and kirigami. *Appl. Phys. Rev.* **8**, 041319 (2021).
2. Jin, L. & Yang, S. Engineering kirigami frameworks toward real-world applications. *Adv. Mater.* **36**, 2308560 (2024).
3. Tao, J., Khosravi, H., Deshpande, V. & Li, S. Engineering by cuts: how kirigami principle enables unique mechanical properties and functionalities. *Adv. Sci.* **10**, 2204733 (2023).
4. Lamoureux, A., Lee, K., Shlian, M., Forrest, S. R. & Shtein, M. Dynamic kirigami structures for integrated solar tracking. *Nat. Commun.* **6**, 8092 (2015).
5. Rafsanjani, A., Zhang, Y., Liu, B., Rubinstein, S. M. & Bertoldi, K. Kirigami skins make a simple soft actuator crawl. *Sci. Robot.* **3**, eaar7555 (2018).
6. Branyan, C., Rafsanjani, A., Bertoldi, K., Hatton, R. L. & Mengüç, Y. Curvilinear kirigami skins let soft bending actuators slither faster. *Front. Robot. AI* **9**, 872007 (2022).
7. Dias, M. A. et al. Kirigami actuators. *Soft Matter* **13**, 9087–9092 (2017).
8. Liu, Z. et al. Nano-kirigami with giant optical chirality. *Sci. Adv.* **4**, eaat4436 (2018).
9. Yang, Y., Vella, K. & Holmes, D. P. Grasping with kirigami shells. *Sci. Robot.* **6**, eabd6426 (2021).
10. Forte, A. E., Melancon, D., Zanati, M., De Giorgi, M. & Bertoldi, K. Chiral mechanical metamaterials for tunable optical transmittance. *Adv. Funct. Mater.* **33**, 2214897 (2023).
11. Choi, G. P. T., Dudte, L. H. & Mahadevan, L. Programming shape using kirigami tessellations. *Nat. Mater.* **18**, 999–1004 (2019).
12. Choi, G. P. T., Dudte, L. H. & Mahadevan, L. Compact reconfigurable kirigami. *Phys. Rev. Res.* **3**, 043030 (2021).
13. Dudte, L. H., Choi, G. P. T., Becker, K. P. & Mahadevan, L. An additive framework for kirigami design. *Nat. Comput. Sci.* **3**, 443–454 (2023).
14. Isobe, M. & Okumura, K. Initial rigid response and softening transition of highly stretchable kirigami sheet materials. *Sci. Rep.* **6**, 24758 (2016).
15. Yang, Y., Dias, M. A. & Holmes, D. P.Multistable kirigami for tunable architected materials. *Phys. Rev. Mater.* **2**, 110601 (2018).
16. Isobe, M. & Okumura, K. Continuity and discontinuity of kirigami's high-extensibility transition: a statistical-physics viewpoint. *Phys. Rev. Res.* **1**, 022001 (2019).
17. Cho, H. & Kim, D.-N. Controlling the stiffness of bistable kirigami surfaces via spatially varying hinges. *Mater. Des.* **231**, 112053 (2023).
18. Tani, M. et al. Curvy cuts: programming axisymmetric kirigami shapes. *Extreme Mech. Lett.* **71**, 102195 (2024).
19. Lamoureux, D., Ramananarivo, SD., Melancon, & Gosselin, F. P. Simulating flow-induced reconfiguration by coupling corotational plate finite elements with a simplified pressure drag. *Extreme Mech. Lett.* **74**, 102271 (2024).
20. White, F. M. & Wolf, D. F. A theory of three-dimensional parachute dynamic stability. *J. Aircr.* **5**, 86–92 (1968).
21. Marzin, T., Le Hay, K., de Langre, E. & Ramananarivo, S. Flow-induced deformation of kirigami sheets. *Phys. Rev. Fluids* **7**, 023906 (2022).
22. Carleton, A. G. & Modarres-Sadeghi, Y. Kirigami sheets in fluid flow. *Extreme Mech. Lett.* **71**, 102198 (2024).
23. Gamble, L., Lamoureux, A. & Shtein, M. Multifunctional composite kirigami skins for aerodynamic control. *Appl. Phys. Lett.* **117**, 254105 (2020).
24. Li, J. et al. Aerodynamics-assisted, efficient and scalable kirigami fog collectors. *Nat. Commun.* **12**, 5484 (2021).
25. Wen, X. et al. Dynamic kirigami structures for wake flow control behind a circular cylinder. *Phys. Fluids* **35**, 011707 (2023).
26. Vogel, S. Drag and reconfiguration of broad leaves in high winds. *J. Exp. Bot.* **40**, 941–948 (1989).
27. Alben, S., Shelley, M. & Zhang, J. Drag reduction through self-similar bending of a flexible body. *Nature* **420**, 479–481 (2002).
28. Schouveiler, L. & Boudaoud, A. The rolling up of sheets in a steady flow. *J. Fluid Mech.* **563**, 71–80 (2006).
29. Gosselin, F., de Langre, E. & Machado-Almeida, B. A. Drag reduction of flexible plates by reconfiguration. *J. Fluid Mech.* **650**, 319–341 (2010).
30. De Langre, E., Gutierrez, A. & Cossé, J. On the scaling of drag reduction by reconfiguration in plants. *C. R. Mec.* **340**, 35–40 (2012).
31. Gosselin, F. P. Mechanics of a plant in fluid flow. *J. Exp. Bot.* **70**, 3533–3548 (2019).
32. Lin, Y. L., Pezzulla, M. & Reis, P. M. Fluid–structure interactions of bristled wings: the trade-off between weight and drag. *J. R. Soc. Interface* **20**, 20230266 (2023).
33. Zhang, X. & Nepf, H. Flow-induced reconfiguration of aquatic plants, including the impact of leaf sheltering. *Limnol. Oceanogr.* **65**, 2697–2712 (2020).
34. Marjoribanks, T. I. & Paul, M. Modelling flow-induced reconfiguration of variable rigidity aquatic vegetation. *J. Hydraul. Res.* **60**, 46–61 (2022).
35. Schouveiler, L. & Eloy, C. Flow-induced draping. *Phys. Rev. Lett.* **111**, 064301 (2013).
36. Gomez, M., Moulton, D. E. & Vella, D.Passive control of viscous flow via elastic snap-through. *Phys. Rev. Lett.* **119**, 144502 (2017).
37. Wang, Z. et al. Towards energy harvesting through flow-induced snap-through oscillations. *Int. J. Mech. Sci.* **254**, 108428 (2023).
38. Minami, S. & Azuma, A. Various flying modes of wind-dispersal seeds. *J. Theor. Biol.* **225**, 1–14 (2003).
39. Biviano, M. D. & Jensen, K. H. Settling aerodynamics is a driver of symmetry in deciduous tree leaves. *J. R. Soc. Interface* **22**, 20240654 (2025).
40. Rafsanjani, A. & Bertoldi, K. Buckling-induced kirigami. *Phys. Rev. Lett.* **118**, 084301 (2017).
41. Hua, R.-N., Zhu, L. & Lu, X.-Y. Dynamics of fluid flow over a circular flexible plate. *J. Fluid Mech.* **759**, 56–72 (2014).
42. Mahadevan, L., Ryu, W. S. & Samuel, A. D. T. Tumbling cards. *Phys. Fluids* **11**, 1–3 (1999).
43. Auguste, F., Magnaudet, J. & Fabre, D. Falling styles of disks. *J. Fluid Mech.* **719**, 388–405 (2013).
44. Li, J. & Liu, Z. Focused-ion-beam-based nano-kirigami: from art to photonics. *Nanophotonics* **7**, 1637–1650 (2018).
45. Sun, Y. et al. Geometric design classification of kirigami-inspired metastructures and metamaterials. *Structures* **33**, 3633–3643 (2021).
46. Guttag, M., Karimi, H. H., Falcón, C. & Reis, P. M. Aeroelastic deformation of a perforated strip. *Phys. Rev. Fluids* **3**, 014003 (2018).
47. Pratap, M., Agrawal, A. K. & Kumar, S. Design and selection criteria of main parachute for re entry space payload. *Def. Sci. J.* **69**, 531–537 (2019).

Methods

Geometric parameters of the closed-loop pattern

The closed-loop kirigami pattern reported in this study can be described by eight independent parameters, that is, $\mathbf{p} = \{r_o, r_i, t, \Delta r_1, \Delta r_2, n, N_\theta, \Theta\}$. The disc is characterized by a thickness t, an outer radius r_o, and an inner hole of radius r_i to impose loading and boundary conditions. The cutting pattern is defined by the number of angular sectors N_θ, the ratio of angular spacing θ_d to angular slits θ_l, that is, $\Theta = \theta_d/\theta_l$, and the radial spacing between two consecutive slits Δr_j with the jth ring forming the closed-loop pattern. The radial slits are spaced from the central hole by an initial distance Δr_1 and the next slit is spaced by Δr_2. The following slits are then made at a spacing given by

$$\Delta r_{j+1} = r_0\left(\left(1+\frac{\Delta r_j}{r_0}\right)^n - 1\right) \forall\, j \geq 2, \tag{1}$$

which is a sequence chosen so that the radial distribution of the cuts could be controlled through a parameter n, where Δr_j is the spacing associated with the last slit cut, slit j. The next slit, $j+1$, will be made at a spacing Δr_{j+1} from slit j. The parameters Δr_2 and Δr_1 are limited by the minimum width possible to cut by the manufacturing method Δr_{min}. The parameter $n \geq 1$ ensures that $\Delta r_j \geq \Delta r_{min} \forall j > 1$. The slits are hereby completely defined radially. We can rewrite equation (1) in the form of a power law as

$$\Delta r_j = r_0\left(\left(1+\frac{\Delta r_2}{r_0}\right)^{n^j} - 1\right), \tag{2}$$

which allows us to solve for the radial position r_j of each slit j using a sum

$$r_j = r_0\left(\sum_{j=0}^{j}\left(1+\frac{\Delta r_2}{r_0}\right)^{n^j} - 1\right). \tag{3}$$

We can also find the number of slits N_r from the parameters Δr_2 and n such that $r_o - r_{Nr} \geq \Delta r_{min}$, which is done using a Python script that automatically generates the cutting pattern. Therefore, the last slit will be distanced from the outer radius by an equal or larger distance than intended, so that $\Delta r_{Nr} \geq \Delta r_{min}$. In the special case in which we choose Δr_j to be constant, therefore $n = 1$, and we want the last blades to have the same with as the previous ones, we need to choose $\Delta r_2 = r_o/N_r$. In this case, equation (2) is simplified to $\Delta r_j = r_o/N_r$, and equation (3) becomes

$$r_j = \frac{j r_0}{N_r}. \tag{4}$$

Here, we consider the general case in which $\Delta r_2 \neq r_o/N_r$ and $n \neq 1$. We note that we normalize the design parameter Δr_2 by the external radius, such that $\Delta x_2 = \Delta r_2/r_o$, which leads to $x_j = r_j/r_o$. Moreover, when considering the slits in the angular direction, we need to specify their number and their width. We decide to keep the angle of the slits constant and therefore define the number of slits in the angular direction as N_θ. Considering the angle of a slit θ_l and the angle of the angular spacing θ_d, we find

$$2\pi = N_\theta(\theta_l + \theta_d) = N_\theta\theta_l(1+\Theta) \rightarrow \theta_l = \frac{2\pi}{N_\theta(1+\Theta)}. \tag{5}$$

The slits are, therefore, completely defined radially and angularly.

Fabrication of kirigami discs

Our kirigami discs and parachutes were made from polyethylene terephthalate, also called Mylar, sheets of varying thicknesses, which remain elastic for large strains. Our Mylar sheets came from a curved roller and, therefore, have an initial curvature that we removed by annealing by leaving the Mylar sheets flat in an oven at 75 °C for an hour, which also removed plasticity effects from the sheets, and letting them rest flat for another hour under a weighted plate outside the oven. Then, the sheets were either cut using a CO_2 cutter (EKO 7, THERMOFLAN) or a laser cutter (Speedy 400 Flexx, TROTEC). For our simulations, we assumed that the cuts made to the kirigami specimens have a width close to 0.1 mm. However, it was observed in a previous study that the width of the cuts at this scale did not affect the kirigami kinematics in an important manner[21], which was confirmed by our observations. A picture of the cutting process as well as the obtained kirigami specimens is shown in Extended Data Fig. 2. Designs A and B of the kirigami discs, used in the drop tests presented in Fig. 1b,c and in the wind tunnel experiments presented in Fig. 2 had a thickness of $t = 69$ μm and an outer radius of $r_o = 70$ mm, with an inner hole of radius $r_i = 3$ mm to attach the payload, which consisted of a screw and a bolt with a mass of 4.5 g. Their cutting parameters are described by $\{\Delta r_1, \Delta r_2, n, N_\theta, \Theta\} = \{3$ mm, 2 mm, 1.0, 8, 0.3$\}$ (design A) and $\{3$ mm, 2 mm, 1.0, 5, 0.3$\}$ (design B). The kirigami specimens used to generate the design space presented in Figs. 3 and 4 were based on the design B kirigami disc, with a single parameter being swept at a time. This leads to the following series:

- Series t: $r_o = 70$ mm, $r_i = 3$ mm, $\Delta r_1 = 6$ mm, $\Delta r_2 = 2$ mm, $n = 1$, $\Theta = 0.3$, $N_\theta = 5$, $t = \{75, 100, 125\}$ μm;
- Series Δr_2: $r_o = 70$ mm, $r_i = 3$ mm, $\Delta r_1 = 6$ mm, $t = 69$ μm, $n = 1$, $\Theta = 0.3$, $N_\theta = 5$, $\Delta r_2 = \{1.5, 2, 2.5, 3, 3.5, 4, 5\}$ mm;
- Series n: $r_o = 70$ mm, $r_i = 3$ mm, $\Delta r_1 = 6$ mm, $\Delta r_2 = 2$ mm, $t = 69$ μm, $\Theta = 0.3$, $N_\theta = 5$, $n = \{1, 1.025, 1.05, 1.075, 1.1, 1.125, 1.15\}$;
- Series Θ: $r_o = 70$ mm, $r_i = 3$ mm, $\Delta r_1 = 6$ mm, $\Delta r_2 = 2$ mm, $t = 69$ μm, $n = 1$, $N_\theta = 5$, $\Theta = \{0.2, 0.25, 0.3, 0.35, 0.4, 0.45\}$;
- Series N_θ: $r_o = 70$ mm, $r_i = 3$ mm, $\Delta r_1 = 6$ mm, $\Delta r_2 = 2$ mm, $t = 69$ μm, $n = 1$, $\Theta = 0.3$, $N_\theta = \{4, 5, 6, 7, 8\}$.

We note that, through our manufacturing process, we identified some manufacturing constraints. First, as discussed, there exists a minimum width Δr_{min} that needs to be used for the radial spacing between the slits. Second, for interactions between the cuts to occur, we need $\Theta \in [0, 1]$ and in order to ensure there is sufficient material between the cuts angularly, we use the same spacing than used radially, leading to the condition

$$N_\theta \leq \frac{2\pi\Delta r_1\Theta}{\Delta r_{min}(1+\Theta)}. \tag{6}$$

We need to respect these conditions; otherwise, our discs tend to break as the material between the slits becomes too thin.

To characterize the mechanical properties of our Mylar sheets, we manufactured different sheets of width $H = 100$ mm, thickness $t = 69$ μm, and initial length $L_0 = 150$ mm. We measured the mass of the sheets and found its density $\rho = 1{,}513.7$ kg m^{-3}. By clamping our sheet at different points along its length or its width, we performed bending tests on three different sheets to measure the bending stiffness B. We also assume a Poisson's ratio $\nu = 0.3$ to identify the Young's modulus E for our simulations. We clamped one end of our sheet and let it bend in a cantilever manner. We measured the length of the sheet that is clamped to find the length of the cantilevered sheet and measure the maximum displacement at the end of the sheet w_{max}. We developed the solution to the maximum displacement of the sheet, as the deformation remains 2D, using the nonlinear Euler–Bernoulli beam equation[29]. By fitting the obtained solution through our measurements as shown in Extended Data Fig. 3, we found a Young's modulus of 6.47 GPa along the length of the sheet and 6.13 GPa along its width. This difference comes from the initial laminated nature of our sheets, causing anisotropy, although the difference remains small here. As our simulations assumed an isotropic material, we instead considered the mean of the Young's moduli $E = 6.3$ GPa.

Fabrication of kirigami-inspired parachutes

To record the lateral, $\ddot{x}$ and $\ddot{y}$, and vertical, $\ddot{z}$, accelerations of the kirigami-inspired parachutes in Fig. 4b, a six-axis accelerometer (AX6 from Axivity) was mounted on the parachutes. For this purpose, larger parachutes inspired by the kirigami disc designs A and B were subjected to laser cutting in polyester plastic sheets. The parachutes had a thickness of $t = 311$ μm and an outer radius $r_o = 215$ mm, with an inner hole of radius $r_i = 21$ mm to attach the payload. The payload consisted of the accelerometer and a water bottle, totalling a mass 0.144 kg. To make sure that the larger parachutes keep the same stiffness of the kirigami disc designs A and B, we adjusted their cutting parameters as described by $\{\Delta r_1, \Delta r_2, n, N_\theta, \Theta\} = \{10\text{ mm}, 6.13\text{ mm}, 1.0, 8, 0.3\}$ (design A), and $\{10\text{ mm}, 6.13\text{ mm}, 1.0, 5, 0.3\}$ (design B).

The kirigami-inspired parachutes used to characterize the lateral drift of designs A and B in Fig. 4c had a thickness of $t = 127$ μm and an outer radius of $r_o = 100$ mm, with an inner hole of radius $r_i = 3$ mm to attach the payload. The payload consisted of a screw and a bolt with a mass of 12.6 g. Their cutting parameters are described by $\{\Delta r_1, \Delta r_2, n, N_\theta, \Theta\} = \{3\text{ mm}, 2.85\text{ mm}, 1.0, 8, 0.3\}$ (design A)} and $\{3\text{ mm}, 2.85\text{ mm}, 1.0, 5, 0.3\}$ (design B).

The large parachute used outdoors presented in Fig. 5 had a thickness of $t = 317.5$ μm and an outer radius of $r_o = 250$ mm, with an inner hole of radius $r_i = 20$ mm to attach the payload. Its cutting parameters are described by $\{\Delta r_1, \Delta r_2, n, N_\theta, \Theta\} = \{10\text{ mm}, 6.21\text{ mm}, 1.0, 9, 0.0758\}$.

We note that all the parachutes and their payload remained intact and did not suffer any breaks or malfunctions during the multiple tests, showing their robustness.

Drop testing of kirigami discs

To obtain the lateral shift of the kirigami discs when free-falling, as discussed in Fig. 1, we perform drop tests in series to find a statistical distribution for each disc. Using the manufactured discs, that is, the plain disc, design A and design B, we place a digital camera (Canon EOS Rebel T4i) in front of a black curtain in a room with good lighting. We use the camera to record the specimens while falling using settings that allow for sharp snapshots, as shown in Fig. 1c–e. We drop the different parachutes 10 times each using the same payload, a screw and a nut, that we switch from one parachute to the other, so that we can perform a statistical analysis on their falling behaviour. To ensure repeatability, we use a small clamp attached to the top of the curtain to indicate the horizontal location of the drop and align the parachute with the top of the curtain visually. To ensure the parachute does not initially start with an angle of attack, we use a string attached to the screw so that the disc remains aligned with the vertical axis. We use MATLAB to convert each snapshot to a grayscale format and extract the pixels that have a higher value than a certain threshold. Moreover, as we aligned the parachutes by hand, we corrected the initial position of the parachute within the software to ensure all parachutes start in the same position so that we can compute the mean and standard deviation of the path of the parachute. The curves of the 10 tests are reported in Extended Data Fig. 1.

Tensile tests

To find the stiffness of our kirigami parachutes, we performed tensile tests at a displacement rate of 2 mm s^{-1}, which we found was sufficiently slow to observe quasi-static deformations and forces, on an Instron 4204 equipped with a 10 N force gauge using a custom 3D printed holder for our discs, forcing them to deform in a mode $\mathcal{K}$ through a traction force in its centre and a clamped perimeter. To estimate the potential hysteresis as well as the error from the tensile test, we manufactured a first specimen, using the same dimensions as design B, and performed three traction cycles, in which we increased and decreased the displacement of the specimen up to $2r_o = 140$ mm, which leads to six force–displacement curves. We plot the mean of these curves along with a shaded area that covers three times its standard deviation in Extended Data Fig. 4a, with a picture of one of the tested specimens during a tensile test in its inset. We observed no noticeable hysteresis, as the shaded area remains relatively small. We note that, as this curve is an average of six other curves, there is little noise observed. We used the specimens manufactured from the previously described series and tested them all to find their force–displacement curve. These specimens observed a first linear behaviour from which a constant stiffness K can be extracted. Extended Data Fig. 4b–f shows the force–displacement curves of the different specimens, arranged by the varied parameter, along with their initial stiffness, using the displacement over their radius to give a better idea of what the displacement represents. The curves did not all reach the same displacements or forces, as we stopped the deformations before the specimen suffered too important deformations, so that it could be reused for other tests. Once a series of tests was performed, we annealed the discs and reused them to ensure that mechanical properties remained the same, rather than manufacturing multiple sets of every specimen.

To compare with the numerical results of our FIRM, we plot the experimental traction curve in Extended Data Fig. 5 for designs A and B, in which the x-axis is the displacement of the centre of the disc w and the y-axis is the traction force F used to deform the disc. We see that the traction curve of design A, which deformed in a mode $\mathcal{C}$ when free-falling, is higher than that of design B, which deformed in mode $\mathcal{K}$. We can also observe that the experimental response of our disc initially follows a linear trend before encountering a nonlinear behaviour at higher displacements. We record this stiffness K, which is $K = 2.606$ N m^{-1} and $K = 0.508$ N m^{-1} for designs A and B, respectively. We compare these experimental traction curves with finite element simulations performed with the FIRM framework in Extended Data Fig. 5 as well. The numerical force–displacement curves of both designs are in overall agreement with the experimental results, with some discrepancies. The simulations for design B predict a smaller force than experimentally recorded, which could be because of experimental errors such that the initial position of the kirigami disc did not generate 0 N. Nevertheless, both curves observe the same behaviour and, most importantly, the numerical simulations predict a stiffness that is close to what is measured experimentally. However, these force–displacement curves describe only the stiffness associated with mode $\mathcal{K}$ as, because of the outer clamp, the disc is forced to elongate. The stiffness associated with mode $\mathcal{C}$, however, is characterized by the bending stiffness $B = Et^3/(12(1-\nu^2))$ of the discs, where E is the Young's modulus and ν is the Poisson's ratio.

Wind tunnel testing

To conduct the wind tunnel experiments presented in Fig. 2, we positioned the kirigami disc perpendicular to the flow in the closed-loop, 61 cm × 61 cm cross-section wind tunnel at Polytechnique Montreal and clamped it at $r_1 = r_i + \Delta r_1$ while leaving the outer radius free. To track deformation and measure aerodynamic forces, we positioned a digital camera (Canon EOS Rebel T4i camera) in front of the test window and connected the sample to a multi-axial load cell (Gamma type from ATI Technologies). During the test, we progressively increase the flow velocity from $U_\infty = [0.61, 10]$ m s^{-1} by intervals of 0.7575 m s^{-1}. The Reynolds number $\mathrm{Re} = 2r_o U_\infty/\nu_a$, where ν_a is the kinematic viscosity of air, reached in the experiments varied in the range of $5{,}600 < \mathrm{Re} < 94{,}000$. We took a snapshot at every increment and recorded the time-average of the forces and moments measured by the load cell over a 30 s period.

To compare the drag of our flexible kirigami discs, we first studied the drag of a rigid disc made of acrylic with a thickness of 3 mm. To maintain the same flow dynamics around the structure, we aimed to keep a small thickness and therefore made the disc of radius $r_o = 68$ mm and attached a flexible disc made out of Mylar of $r_o = 70$ mm and thickness $t = 69$ μm in front of it. Owing to the large, rigid support behind the flexible disc, its behaviour remained similar to a rigid disc. Extended Data Fig. 6a shows the total measured drag of this rigid disc D, the

contribution from the isolated stand and the isolated drag of the specimen once we remove the contribution of the stand from the total measurement according to the velocity U_∞. This allows us to compare our flexible disc with a rigid reference. Here, we considered that the slits in the kirigami discs did not modify the drag of their rigid counterpart drastically. Moreover, with the drag generated by the stand, we isolated the drag generated by the flexible kirigami specimens. Extended Data Fig. 6b–f shows the drag of a limited number of our previously manufactured discs that deform in mode $\mathcal{K}$, arranged according to the varied parameter. From these tests, we also took pictures of our specimens to extract their elongation along the flow stream (Extended Data Fig. 7a). By converting the image to a grayscale format and filtering the pixels that are darker than a certain threshold, we isolated the specimen in the picture and measured its deformed length. We plot the elongation of all the previously tested specimens, arranged according to their varied parameter (Extended Data Fig. 7b–f).

FIRM framework

The FIRM framework is a finite element simulation software based on a corotational formulation of plate elements that uses a semi-empirical momentum conservation formulation to approximate the flow load on a flexible structure. Through momentum conservation, we find that the local applied pressure field p on a small element follows $p = \rho U_\infty^2 C_D \cos^2\beta/2$, where ρ is the fluid density, U_∞ is the flow velocity, C_D is the drag coefficient of the rigid structure, and β is the angle the normal of the surface of the element makes with the flow[19,28,29,35]. During wind tunnel experiments, we noted that, whereas the simulations for design A did not require any modification to the FIRM framework, design B showed a high porosity, especially at high values of U_∞ (as evident from the pores created by the structure deploying in Fig. 2b). This led to a more complex flow regime around the structure than the uniform flow assumed by FIRM. To account for this effect, we implemented a porosity model based on ref. 46, in which the area opened through the pores in the structure reduces the effective drag coefficient of the structure (Supplementary Methods, section S1, for more details).

Terminal velocity of Kirigami-inspired parachutes

To conduct the outdoor drop tests with the large kirigami-inspired parachute, we used a payload consisting of a water bottle weighing 0.401 kg equipped with a GoPro camera (Black 11 weighing 0.253 kg). Note that the weight of the parachute itself is 0.08 kg. Based on the total weight of 0.734 kg, we expect a terminal velocity of 11.66 m s^{-1} and an elongation of 0.54 m, which is found at $C_\gamma = 1.804$ using the FIRM prediction with the added porosity model. Figure 5c shows that the kirigami parachute is highly deformed but remains in the predicted Cauchy range. We note that winds were present during testing, causing relatively important lateral accelerations that are not modelled in our simulations. These winds caused angular vibrations of the water bottle, which were damped by the interaction of the parachute with the flow. Nevertheless, the kirigami-inspired parachute fell vertically and did not deviate substantially from its axis (we estimated a lateral displacement of about 7 m over the 60-m free fall based on the GoPro attached to the parachute; Supplementary Video 4). Using Fig. 5c, we can estimate the falling velocity using the elongation of the parachute. Although we expected an elongation of 0.54 m, we observed an elongation in the range of [0.572, 0.685] m. The pattern of the parachute has a maximum elongation $r_o l = 1.4232$ m, leading to $\delta = [0.402, 0.481]$, which is found in the range $C_\gamma = [2.0713, 3.2754]$ using the elongation solution of the FIRM with the porosity model. We, therefore, find that the mean velocity is $U_\infty = 14.11$ m s^{-1}. The velocity we find is slightly higher than predicted, with an error of 21.01%. However, the method with which we estimated the terminal velocity here led to potential errors due to scaling and orientation uncertainties. Nevertheless, the parachute does slow down the water bottle from reaching a free-fall velocity, and, although the scale at which this parachute operates is different from the specimens studied in the wind tunnel, we still find a similar performance to what we predicted.

Tumbling of kirigami-inspired parachutes

To investigate the tumbling frequency of our parachute, we conducted drop tests for parachutes with designs A and B cut patterns. The parachutes were manufactured from a 0.311 mm thick shim with outer radius of $r_o = 215$ mm and inner radius of $r_i = 21$ mm. We mounted a six-axis accelerometer (Ax6 from Axivity) on the parachutes and dropped them indoors from a height of 14.9 m while measuring their linear accelerations, $\ddot{x}$, $\ddot{y}$ and $\ddot{z}$ at a sampling rate of 200 Hz. Extended Data Fig. 8 shows the magnitude of the lateral acceleration, that is, $\ddot{r} = (\ddot{x}^2 + \ddot{y}^2)^{1/2}$, as a function of time during the fall. For design A deforming in mode $\mathcal{C}$ (blue curve in Extended Data Fig. 8a), no distinct pattern emerged in the signal. By contrast, for design B deforming in mode $\mathcal{K}$ (green curve in Extended Data Fig. 8b), we see a distinct frequency emerging. To extract the tumbling frequency from the raw accelerometer data, we used the autocorrelation function:

$$R(\tau) = \frac{1}{N-\tau} \sum_{t=0}^{N-\tau-1} \ddot{r}(t) \cdot \ddot{r}(t+\tau), \tag{7}$$

where N is the total number of samples and τ is the time lag. To determine the frequency of a signal using this method, we computed the $R(\tau)$ for different values of τ and identified the highest peak following the initial maximum at $\tau = 0$. This peak represents the fundamental periodicity of the signal, as it indicates the time shift at which the signal best aligns with itself. By applying this method to each of the three tests conducted on design B, we found tumbling frequencies of 1.40 Hz, 1.39 Hz and 1.48 Hz for an average frequency of 1.42 Hz. Simplifying the problem to the swing of a simple gravity pendulum with frequency equal to $f_p = 1/2\pi(g/l_p)^{1/2}$, where g is the acceleration of gravity and l_p is the length of the pendulum, which we assume is of the same order as the disc radius, that is, $l_p = r_o = 0.215$ mm, we find $f_p = 1.08$ Hz, which is very close to the measured value of $f = 1.42$ Hz. We propose that our kirigami parachutes deforming in mode $\mathcal{K}$ sways at frequency $f \sim 1/2\pi(g/r_o)^{1/2}$.

Drop testing of a conventional parachute

To compare the behaviour of our kirigami-inspired parachutes with a conventional parachute, we conducted similar drop experiments to the ones we conducted on designs A and B cut patterns. We used a conventional elliptical parachute manufactured by Fruity Chutes with $r_o = 195$ mm, $r_i = 24$ mm and a drag coefficient of $C_D = 1.5$. First, the parachute was dropped indoors from a height of 14.9 m, while being equipped with a 6-axis accelerometer (AX6 from Axivity). The accelerometer measured the vertical acceleration $\ddot{z}$ of the parachute at a sampling rate of 200 Hz. Extended Data Fig. 9a shows the vertical acceleration measured over three tests as a function of time (solid curve). We observed that the conventional parachute descended with an unsteady vertical acceleration, similar to design A deforming in mode $\mathcal{C}$. By integrating the average of the vertical acceleration $\ddot{z}$, we obtained the vertical velocity $\dot{z}$ over time (dashed curve in Extended Data Fig. 9a). The terminal velocity of the conventional parachute was calculated as −4.66 m s^{-1}. In Extended Data Fig. 9b, we report the lateral displacement of the fall across eight drop tests. We found a large discrepancy with one parachute falling more than 10 m away from the target.

Data availability

All wind-tunnel and tensile testing raw data are included as Supplementary Data 1 and 2. The FIRM is openly available at GitHub (https://github.com/lm2-poly/FIRM).

Acknowledgements We thank C. Adler and M. Wierre for performing initial experimental tests of reconfigurable kirigami structures. D.L. acknowledges Y. Liétard for assembling the large-scale parachute, as well as G. Beltrame, H. M. Bong, M. Boukor, J. Garon, P. Gerard, A. Sibille and M. Verville for their help in testing the large-scale parachutes. We acknowledge the financial support of the Natural Sciences and Engineering Research Council of Canada (funding reference nos. RGPIN-2019-7072 and RGPIN-2023-04463). D.L. acknowledges funding by a NSERC BESC-M scholarship, the Supplément pour Études à l'Étranger BESC-SEEMS of NSERC, and a master's scholarship of Fonds de Recherche du Québec—Nature et Technologies. S.R. acknowledges support from a JCJC grant of the Agence Nationale de la Recherche (ANR-20-CE30-0009-01).

Author contributions D.L., S.R., F.P.G. and D.M. proposed and developed the research idea. D.L. designed, fabricated and tested the kirigami disks and parachutes for the initial submission of the manuscript. J.F. fabricated the kirigami parachutes for the revised version of the manuscript. D.L. conducted the numerical simulations. D.L., J.F., S.R., F.P.G. and D.M. wrote the paper. S.R., F.P.G. and D.M. supervised the research.

Competing interests The authors declare no competing interests.

Additional information

Supplementary information The online version contains supplementary material available at https://doi.org/10.1038/s41586-025-09515-9.

Correspondence and requests for materials should be addressed to Frédérick P. Gosselin or David Melancon.

Peer review information *Nature* thanks the anonymous reviewer(s) for their contribution to the peer review of this work. Peer reviewer reports are available.

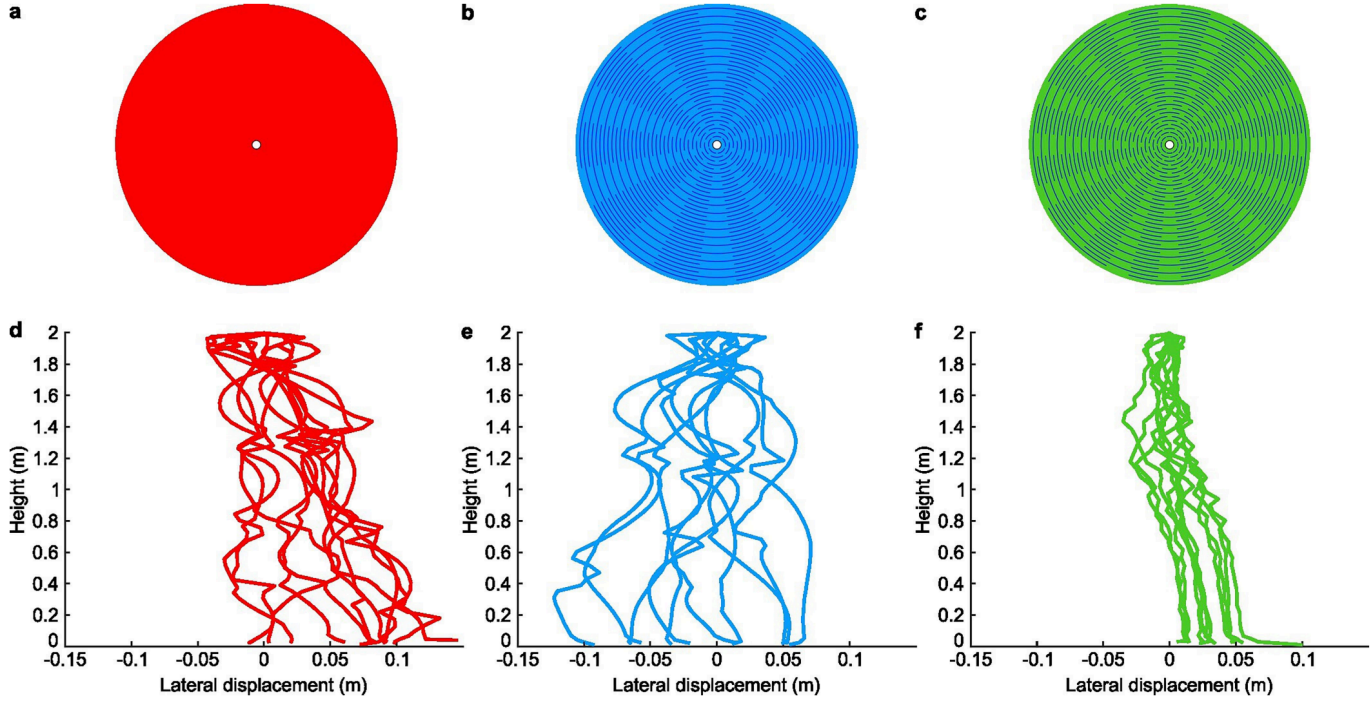

Extended Data Fig. 1 | Lateral displacement of plain and kirigami disks during free fall. a. Plain circular disk. **b**. Cutting pattern of kirigami disk Design A. **c**. Cutting pattern of kirigami disk Design B. **d**. Lateral displacement as a function of vertical height during free fall for ten disks with no cuts (**d**), ten disks with cutting pattern Design A (**e**), and ten disks with cutting pattern Design B (**f**).

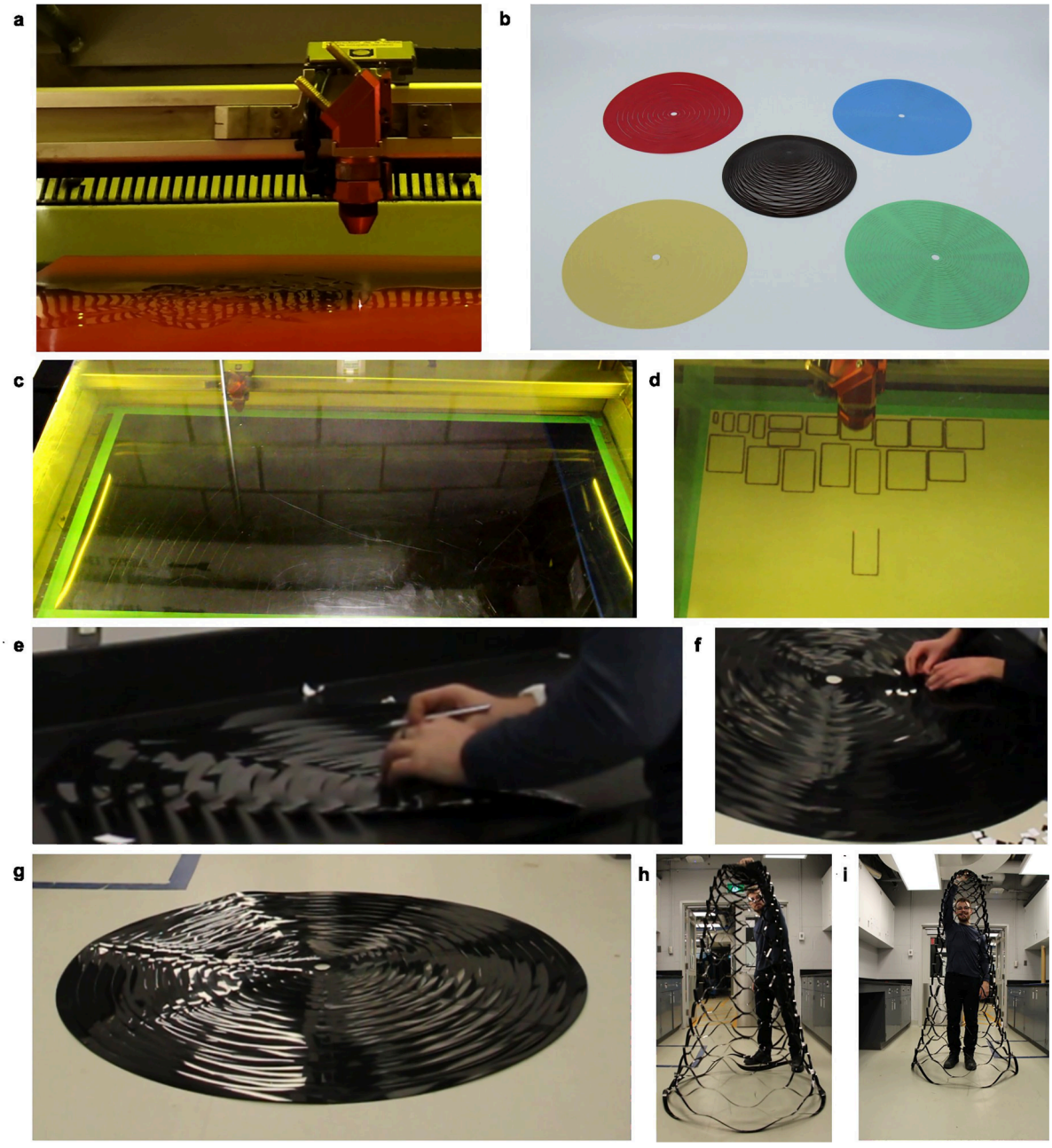

Extended Data Fig. 2 | Manufacturing method for both small and meter-scale parachutes. a. Laser cutting process using the TROTEC Speedy 400 Flexx, leading to (**b**) small parachute specimens. **b**. Laser cutting of large parachute specimen sectors and **c**. adhesive patches to link the parachute sectors. **e**. Assembly method between two sectors leading to **f**. assembling the patched sectors into the whole parachute. **g**. Complete assembled meter-scale parachute **h**. observing mode $\mathcal{K}$ under its own weight up to **i**. the height of one of the authors.

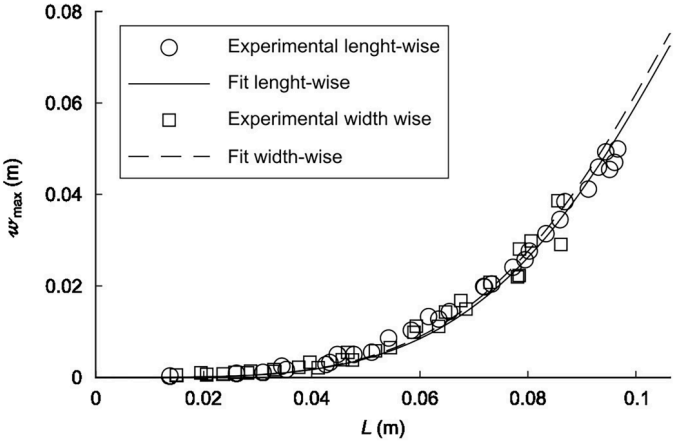

Extended Data Fig. 3 | Mechanical characterization of the base material. Maximum displacement w_{max} of different Mylar sheets of lengths L obtained through bending tests. Due to the laminated nature of the sheet, an anisotropy is obtained when the sheet is bending in different directions, which is illustrated through the different fits.

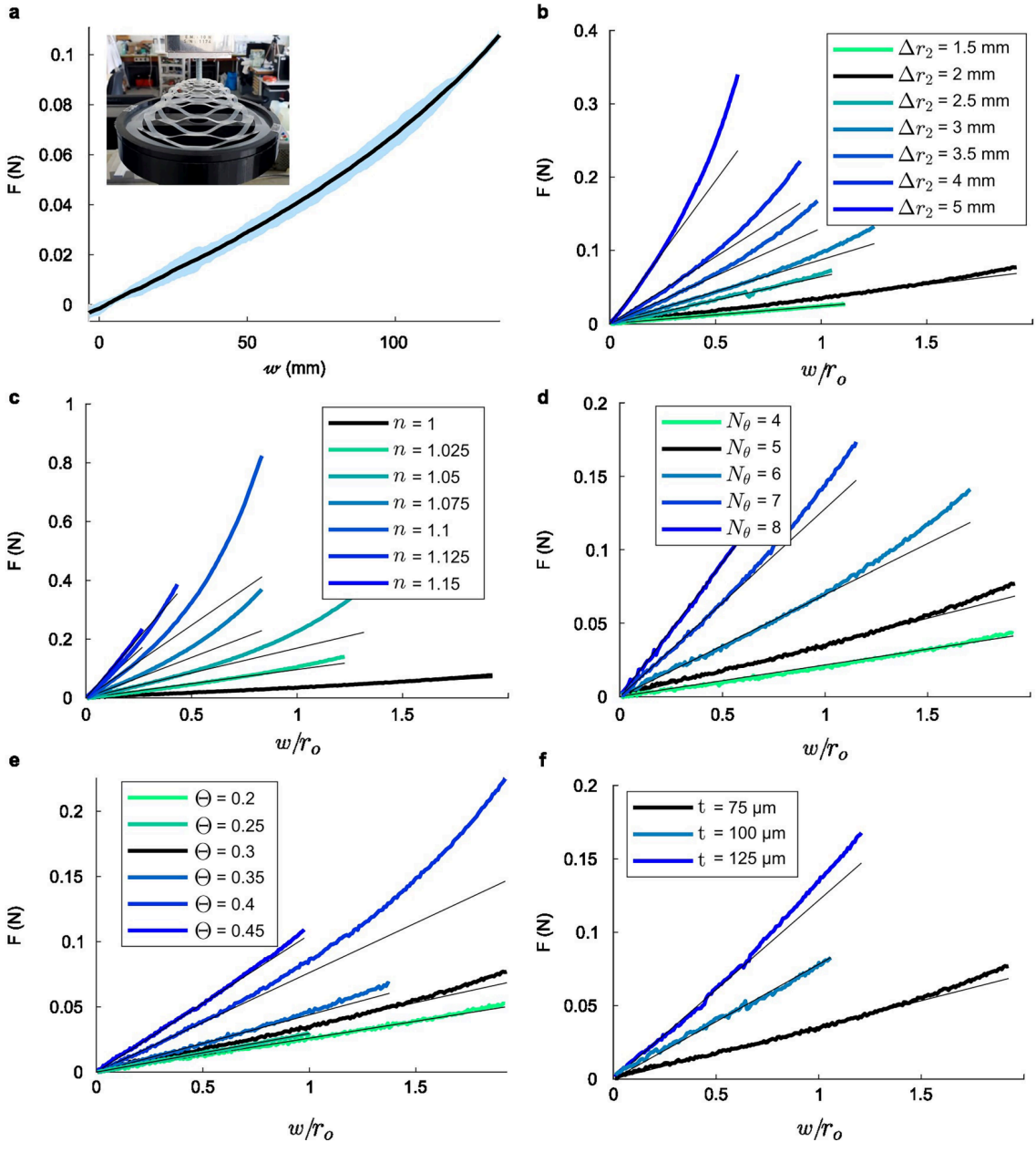

Extended Data Fig. 4 | Force-displacement curves of different closed-loop kirigami specimens. a. Hysteresis and error of the force-displacement curve of the Design B kirigami disk. The line shows the average of six force-displacement curves over three traction cycles while the shaded area shows three times the standard deviation. **b**-**f**. The force-displacement curves of the specimens with varied **b**. radial spacing Δr_2, **c**. radial distribution exponent n, **d**. number of angular sectors N_θ, **e**. cutting ratio Θ and **f**. thickness t also present initial stiffnesses of the tested specimens.

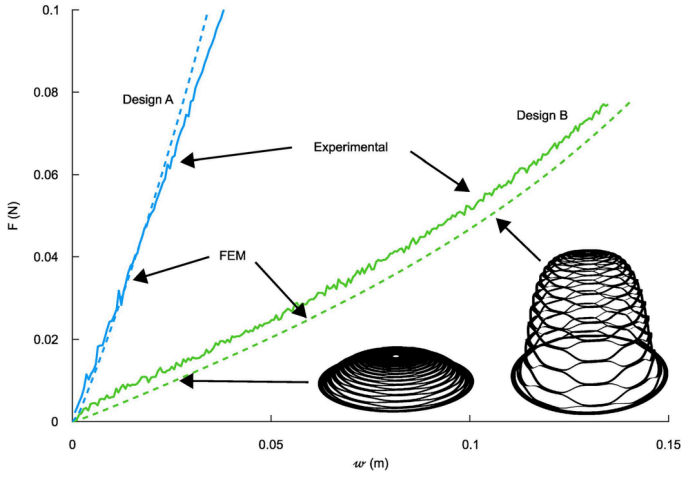

Extended Data Fig. 5 | Comparison between experimental and numerical force-displacement curves of Design B. Force applied F to the kirigami disk designs to obtain the displacement of the center w using experiments and numerical simulations. Accompanying images show the deformed shape of Design B at different displacements, which are similar to the deformed shapes of Design A, as the deformation is forced to be in mode $\mathcal{K}$.

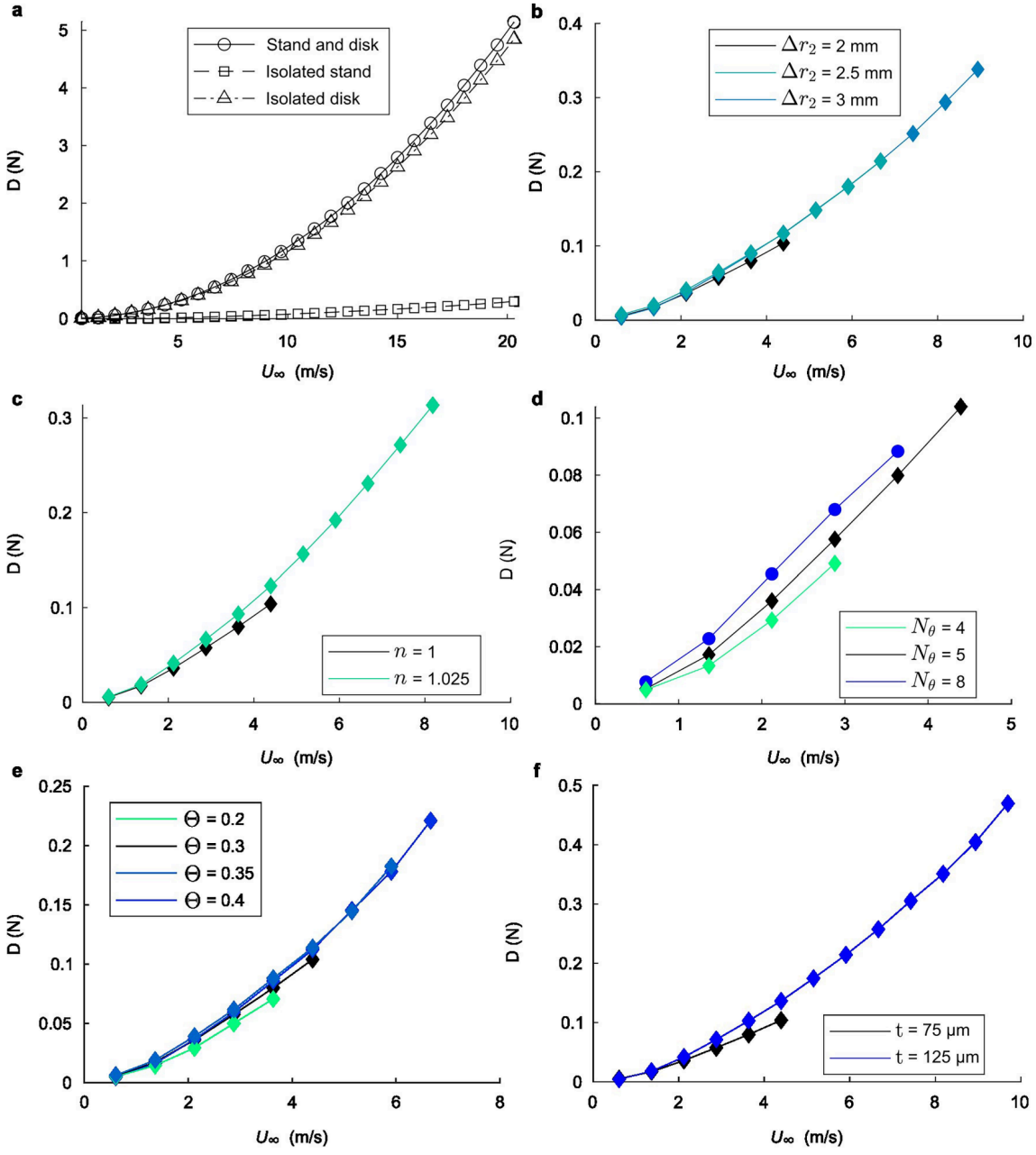

Extended Data Fig. 6 | Drag of the kirigami specimens D according to the flow velocity U_∞. a. Total measured drag of a rigid disk along with the contributions from the stand and the isolated specimen. **b**-**f.** The drag-velocity curves of the specimens with with varied **b.** radial spacing Δr_2, **c.** radial distribution exponent n, **d.** number of angular sectors N_θ, **e.** cutting ratio Θ and **f.** thickness t, where the markers show the deformation mode (diamonds are mode $\mathcal{K}$ and circles is mode $\mathcal{C}$).

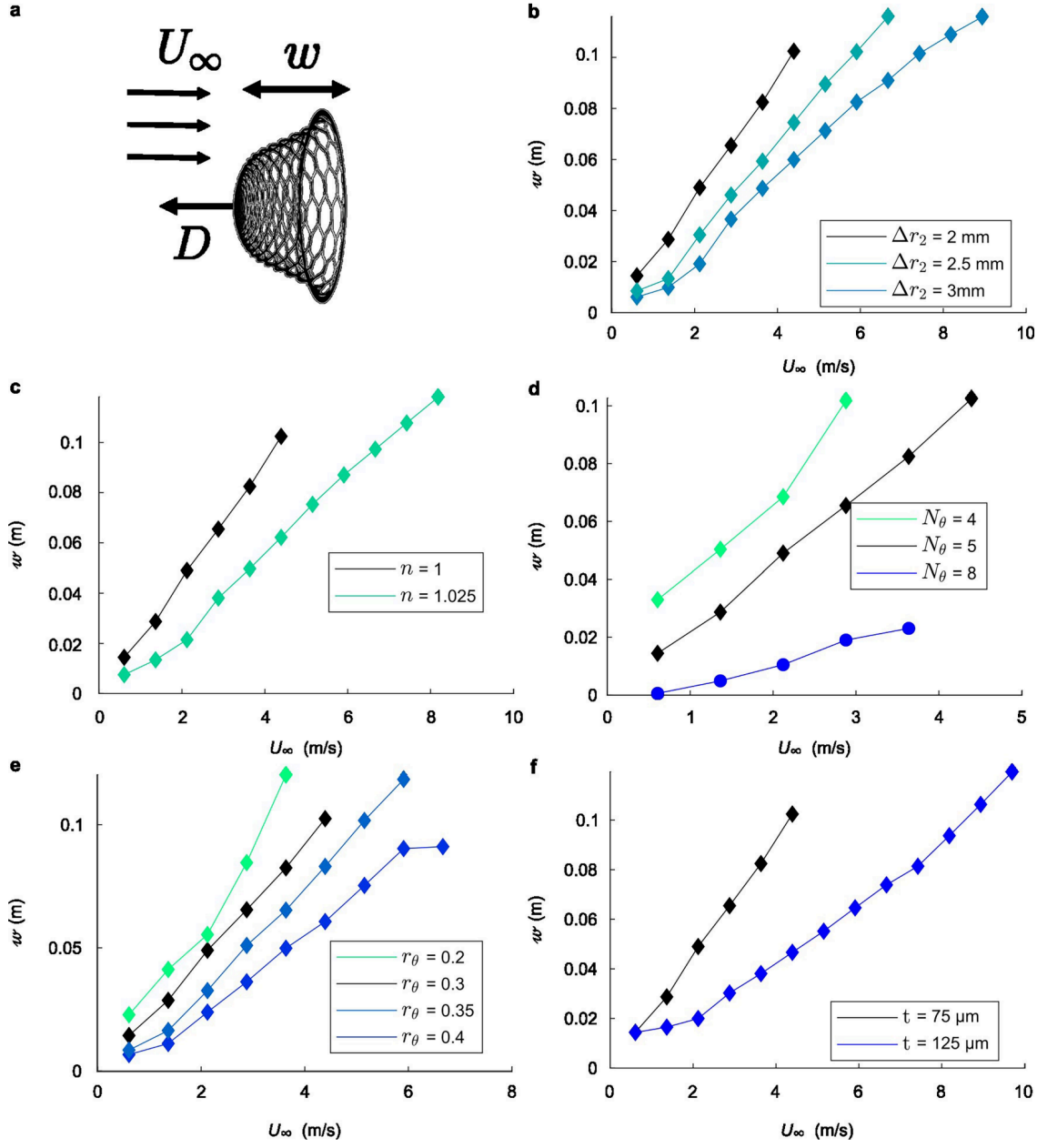

Extended Data Fig. 7 | Elongation of the kirigami specimens w under flow velocity U_∞. **a.** Schematic of the deformed kirigami disk. **b-f.** Displacement-velocity curves of the specimens with with varied **b.** radial spacing Δr_2, **c.** radial distribution exponent n, **d.** number of angular sectors N_θ, **e.** cutting ratio Θ and **f.** thickness t, where the markers show the deformation mode (diamonds are mode $\mathcal{K}$ and circles is mode $\mathcal{C}$).

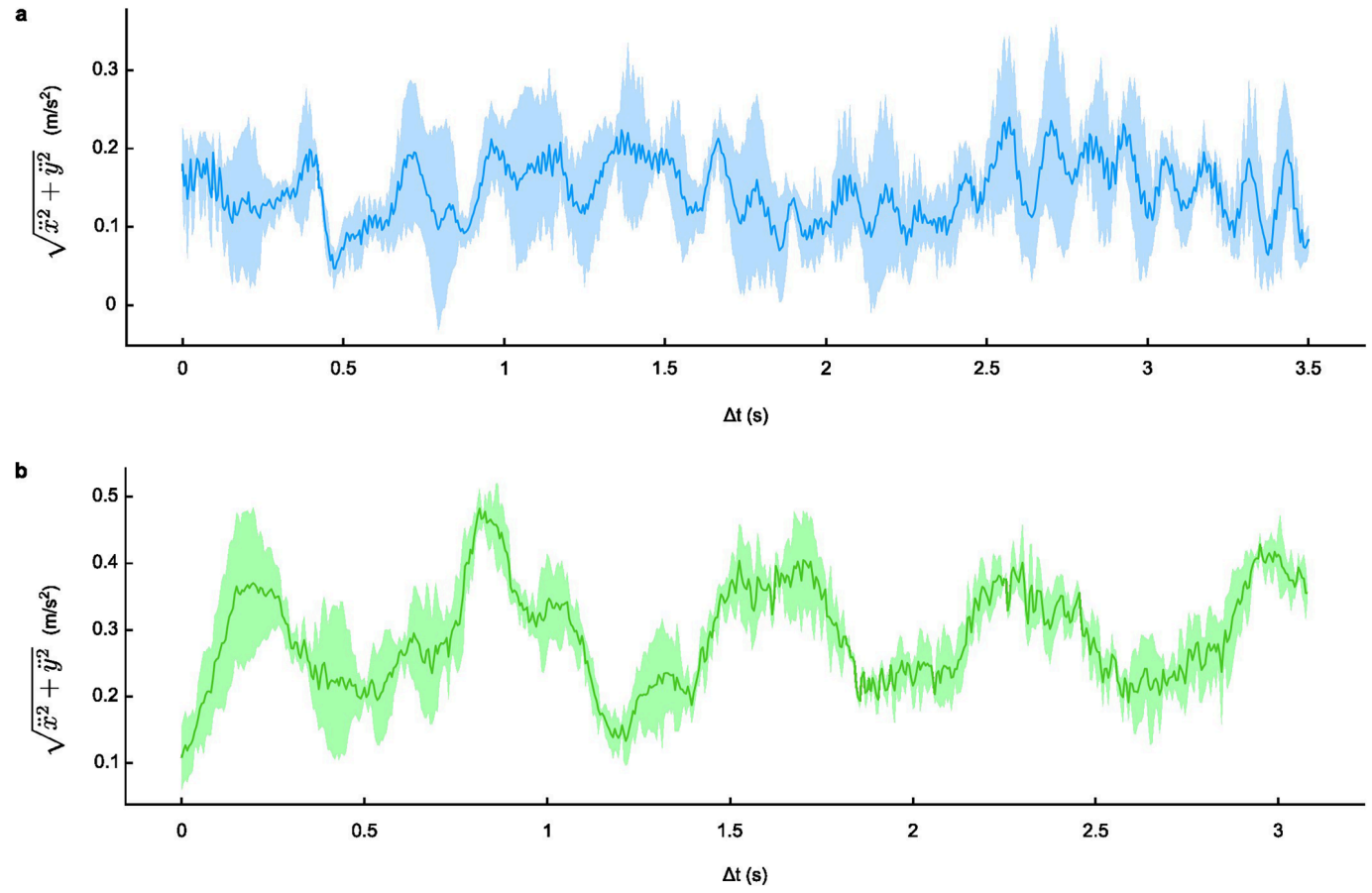

Extended Data Fig. 8 | Magnitude of the lateral acceleration as a function of time during fall. a. Results for Design A deforming in the cylindrical mode $\mathcal{C}$. **b**. Results for Design B deforming in the kirigami mode $\mathcal{K}$. The lines and shaded areas are the average and standard deviation of three fall experiments.

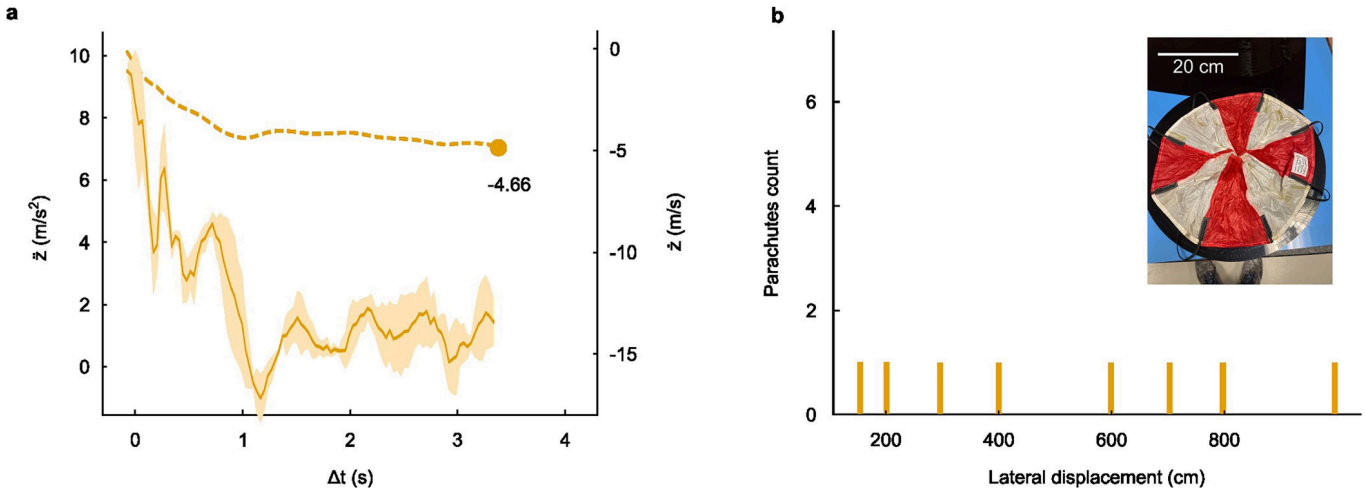

Extended Data Fig. 9 | Performance of a conventional parachute. a. Vertical acceleration, $\ddot{z}$, and velocity, $\dot{z}$, of the conventional parachute. The solid line and shaded area are the average and standard deviation of the vertical acceleration of three fall experiments measured with an accelerometer. The dashed line is the vertical velocity obtained by integrating numerically the mean vertical acceleration of three fall experiments. **b.** Lateral displacement of the conventional parachute across multiple drop tests. Inset shows the parachute by *Fruity Chutes*.